LASER & PHOTONICS REVIEWS

**Abstract** The state-of-the-art of high-refractive-index-contrast single-crystalline thin lithium niobate ($LiNbO_3$) films as a new platform for high-density integrated optics is reviewed. Sub-micrometer thin $LiNbO_3$ films are obtained by "ion-slicing". They can be bonded by two different techniques to a low-index substrate to obtain "lithium niobate on insulator" (LNOI) even as wafer of $3''$ diameter. Different micro- and nano-structuring techniques have been used to successfully develop micro-photonic devices. To be specific, the fabrication and characterization of LNOI photonic wires with cross-section $< 1\,\mu m^2$, periodically poled LNOI photonic wires for second harmonic generation, electro-optically tunable microring resonators, free standing microrings for hybrid integration, and photonic crystal structures are described.
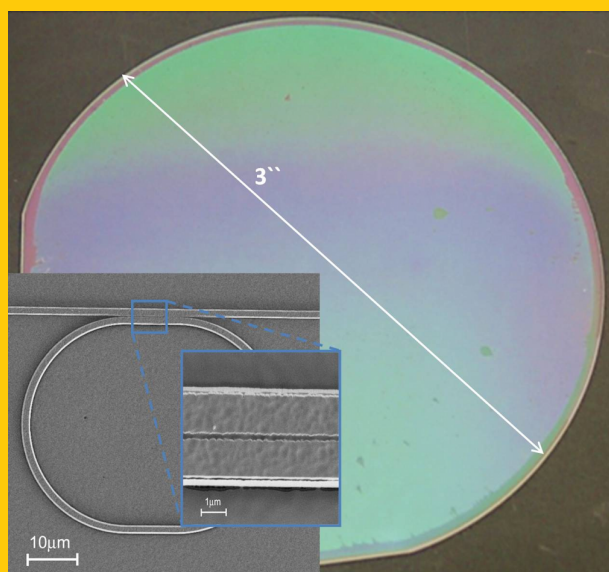
Lithium niobate on insulator (LNOI) for micro-photonic devices

Gorazd Poberaj [1,3,*], **Hui Hu** [2,4], **Wolfgang Sohler** [2], **and Peter Günter** [1,5]

1. Introduction

As optical components continue to replace electronics for optical signal processing applications, there is a growing impetus to integrate more photonic devices onto a single chip. Compared to electronics, photonic devices offer several advantages, such as large bandwidth operation, wavelength division multiplexing, and also absence of electro-magnetic interference. In the last few years, strong efforts have been made to develop silicon based photonic chips [1]. This field of research has profited considerably from the availability of large-size silicon-on-insulator (SOI) wafers and the advanced semiconductor technology providing solutions for micro- and nano-structuring of photonic devices. A high refractive index contrast between silicon and silicon-oxide is essential for the realization of highly integrated optics devices based on photonic wires [2–4] and photonic band gap structures [5]. SOI photonic wires can have a very small cross-section (even below $1\,\mu m^2$) and also small bending radius ($\sim 10\,\mu m$).

A corresponding technology for lithium niobate ($LiNbO_3$) is still in its infancy, though $LiNbO_3$ offers – in contrast to SOI – excellent electro-optic, acousto-optic, and nonlinear

optical properties. Moreover, it can be easily doped with rare-earth ions to get a laser active material [6]. Therefore, $LiNbO_3$ photonic wires will enable the development of a wide range of extremely compact, active integrated devices, including electro-optical modulators, tunable filters, nonlinear wavelength converters, and amplifiers and (tunable) lasers of different types. In particular, periodically poled $LiNbO_3$ (PPLN) photonic wires are ideal candidates for extremely efficient nonlinear optical devices for wavelength conversion and all-optical signal processing.

The key step towards realization of high-index-contrast $LiNbO_3$ waveguides is to produce single-crystalline $LiNbO_3$ thin films, which can be structured and embedded in low index dielectric materials. In this endeavor, many techniques have been studied in the past, such as chemical vapor deposition [7], RF sputtering [8], molecular beam epitaxy [9], sol-gel [10], and pulsed laser deposition [11]. However, all these techniques have difficulty in producing high crystalline quality materials. In addition, the use of substrates with required properties is limited, in particular for epitaxial growth due to lattice matching constraints. More recently, crystal ion slicing in combination with wafer bonding techniques has emerged as a very promising technique for fab-

[1] Nonlinear Optics Laboratory, Institute of Quantum Electronics, ETH Zurich, 8093 Zurich, Switzerland   [2] Angewandte Physik, Universität Paderborn, Warburger Strasse 100, 33098 Paderborn, Germany   [3] Present affiliation: Onefive GmbH, 8046 Zürich, Switzerland   [4] Present affiliation: School of Physics and Microelectronics, Shandong University, Jinan, Shandong 250100, China   [5] Now also with Rainbow Photonics Ltd, 8049 Zürich, Switzerland
[*] Corresponding author: e-mail: poberaj@phys.ethz.ch

rication of single-crystalline ferroelectric thin films. This method generally known under the name of "Smart Cut" was originally discovered and applied for the fabrication of SOI wafers [12]. It uses high-dose implantations of H^+ and/or He^+ ions (dose $D \sim 10^{16}$–10^{17}/cm^2) for cleaving films from a bulk material. Since the process was disclosed in 1995 [13], several variants of this method have also been studied for the exfoliation and transfer of different ferroelectric thin films.

Using crystal ion slicing technology, free-standing LiNbO$_3$ films with areas of several cm^2 were successfully fabricated and devices were demonstrated [14]. Crystal ion slicing was combined with direct bonding to fabricate LiNbO$_3$ films on SiO$_2$ of an area of ~ 1 cm^2 [15]. Using benzocyclobutene (BCB) as cladding layer, LiNbO$_3$ films of a size of several cm^2 were realized and electro-optical tunable micro-ring resonators were reported [16]. Recently, a full wafer technology to fabricate single crystalline LiNbO$_3$ layers of sub-micrometer thickness on a vacuum deposited SiO$_2$ layer on a LiNbO$_3$ substrate has been developed [17]. In contrast to the BCB bonded material, annealing at much higher temperatures is possible. High temperature annealing can minimize ion-implantation induced material damage and helps to recover electro- and nonlinear optical properties [18, 19]. Moreover, high temperature annealing contributes significantly to a reduction of the surface roughness of LiNbO$_3$ ridge waveguides.

This paper is structured as follows. Section 2 describes the fabrication of ion-sliced lithium niobate thin films. In particular, it reviews two different techniques for bonding submicrometer ion-sliced LiNbO$_3$ films on low-index substrates to obtain "lithium niobate on insulator" (LNOI) samples and even wafers. Section 3 focuses on micro- and nanostructuring techniques which have been developed for prototyping of high density integrated optical devices in LNOI. The first low-loss and even periodically poled photonic wires in LNOI are presented in Sect. 4. Section 5 reviews the first realization of electro-optically tunable microring resonators. Section 6 demonstrates the suitability of LNOI as a platform for photonic crystal structures. Section 7 concludes the review and gives prospects for future developments of high-density integrated optics devices based on LNOI.

2. Fabrication of LNOI

The first step to fabricate LNOI consists of "ion-slicing" a thin film of LiNbO$_3$ from a single crystalline LiNbO$_3$ sample. A high-dose implantation with He^+ ions is used to define a "cleavage plane" within the crystal (Sect. 2.1).

Before cleaving is done by a special annealing process, the ion-implanted crystal is bonded to a substrate. Two different techniques for bonding on low-index substrates have been developed to obtain high quality LNOI samples and even full wafers.

In the first approach, bonding is performed using BCB on a LiNbO$_3$ substrate, which turned out to be a very reliable and reproducible way for the fabrication of large-area (several cm^2) LNOI samples. Using a polymer adhesive has the

advantage of substantially relaxed requirements for flatness, roughness, and cleanliness of the bonded surfaces. Prior to bonding, the LiNbO$_3$ substrate can also be coated with a thin metal layer serving as bottom electrode in electro-optically active devices (Sect. 2.2).

In the second approach, crystal bonding to SiO$_2$-coated LiNbO$_3$ was used to fabricate LNOI. In contrast to the BCB bonded material, annealing at much higher temperatures is possible. This is important to recover electro- and nonlinear optical properties of the cleaved LiNbO$_3$ film. Moreover, high temperature annealing significantly reduces the surface roughness of ion beam etched LiNbO$_3$ (Sect. 2.3).

Crystal bonding is a very versatile process. It was also used to fabricate various sandwich structures with a thin metal electrode either underneath the SiO$_2$ layer or underneath the LiNbO$_3$ film; such structures should enable electric field induced poling and electro-optic control of light propagation. Also LNOI samples with MgO-doped LiNbO$_3$ core layers have been developed (Sect. 2.4).

2.1. Crystal ion slicing

The crystal ion slicing technique is based on high dose ion implantation and epitaxial lift-off. Several studies [14, 15, 20–23] have shown that He^+ implantation is suitable for slicing of LiNbO$_3$. In the implanted layer, He forms gaseous bubbles, also referred to as blisters. Basically, thin film exfoliation or lift-off from an implanted LiNbO$_3$ crystal can be achieved either by wet-etching [20, 24] or thermal treatment [15, 21]. The reported methods differ also in bonding techniques used for the transfer of brittle exfoliated thin films onto supporting substrates. Bonding is one of the most critical steps in fabrication of large-area thin films.

The wet-etching technique exploits selective etching: the ion implanted damaged layer (induced at the ion penetration depth) can be etched by HF with much higher rates than undamaged, crystalline LiNbO$_3$. An etching selectivity as high as 10 000 has been reported for an optimized process [25]. The final bonding of the detached film on the support substrate can be performed after etching and annealing, so that any extensive thermal cycling of the film/substrate composite can be avoided. However, this method is limited to films of many micrometer thickness. They vary continually and gradually in thickness, being thicker in the center and thinner towards the edges, where the exposure to HF was longer [24].

In order to fabricate uniform sub-micrometer thin LiNbO$_3$ films, thermally induced exfoliation has been used. Thermal treatment induces a growth of microcavities in the damaged layer, leading to micro-cracks and finally to a detachment of the implanted layer. A controlled split-off or exfoliation is possible only after proper bonding of the implanted sample onto a supporting substrate. Since the thermal treatment requires elevated temperatures (> 220 °C) for the exfoliation of implanted LiNbO$_3$ crystals, the different thermal expansion of the bonded materials is a very critical issue. A thermal expansion mismatch can induce a large
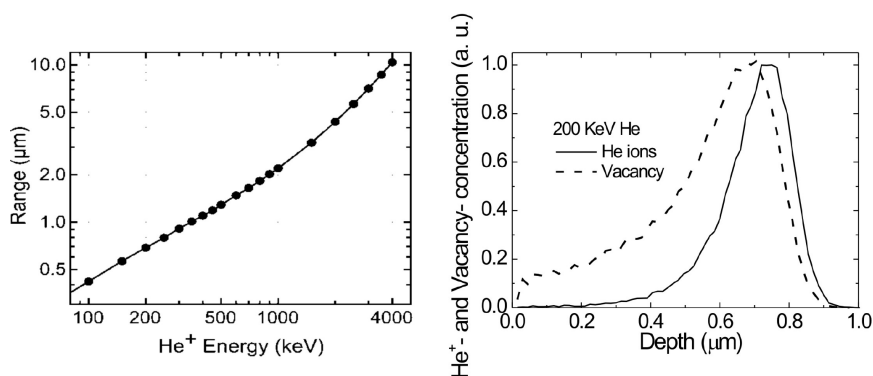
Figure 1 Left: Calculated range of He$^+$ ions implanted into lithium niobate as function of their energy [29]. Right: He$^+$- and vacancy-distributions calculated by SRIM.

mechanical stress, causing cracks and voids in the transferred film. In the following subsections, two techniques are described, which have successfully overcome this problem.

Since the thickness of an ion-sliced film is determined by the implantation depth of the implanted He$^+$ ions, the required film thickness for a particular application can be adjusted by the implantation energy. Figure 1 shows an average penetration depth (range) of implanted He$^+$ ions in LiNbO$_3$ as function of their energy according to "Stopping and Range of Ions in Matter" (SRIM) calculations [26]. An implantation energy of ~ 200 keV is suitable for ion-slicing of sub-micrometer thin layers. The obtained planar LiNbO$_3$ waveguides on a low index cladding support single transverse modes (in vertical direction) at 1550 nm wavelength.

2.2. BCB bonding

In this approach, developed at ETH Zurich [16], the bonding is performed using an adhesive polymer benzocyclobutene (BCB) [27, 28], which turned out to be a very reliable and reproducible way for fabrication of large-area (several cm^2) LiNbO$_3$ thin films. Using a polymer adhesive has the advantage of substantially relaxed requirements for the flatness, roughness, and cleanliness of the bonded surfaces (donor and acceptor wafer). Optically, BCB has excellent transparency in the visible and infrared region, and as a cladding layer provides a suitable optical confinement owing to its low refractive index ($n \approx 1.55$).

The whole fabrication procedure [16, 29] is schematically shown in Fig. 2. A Z- or X-cut congruent LiNbO$_3$ wafer with a diameter of $3''$ and a thickness of 0.5 mm is implanted with He$^+$ ions with an energy of 195 keV and a dose of $\sim 4.5 \times 10^{16}$ cm^{-2}. The implanted wafer is then cut into smaller samples, which are cleaned using standard RCA1 solution and bonded to LiNbO$_3$ substrates by means of BCB. Prior to the bonding, the substrates can also be coated with a thin metal layer (e.g., 50 nm of Cr) serving as a bottom electrode in electro-optically active devices. After the bonding, the sample is gradually heated up. The thermal treatment has a threefold role: in the slow-ramp heating phase the bonding strength is increased, at around 220 °C the implanted layer splits-off from the donor wafer as a single-crystalline film, and this is then annealed at 300 °C for several hours to partially recover implantation-induced crystal defects. Finally,
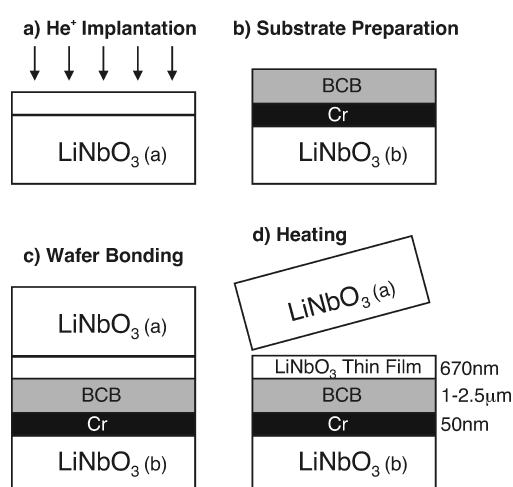

Figure 2 Schematic of the LiNbO$_3$ thin film fabrication method: (a) He$^+$ implantation of LiNbO$_3$ donor wafer ($E = 195$ keV, $D \sim 4.5 \times 10^{16}$ cm^{-2}); (b) preparation of LiNbO$_3$ receptor wafer (substrate); deposition of Cr electrode and spin coating of an adhesive polymer film (BCB); (c) wafer bonding; (d) slow-ramp thermal treatment: strong bonding, LiNbO$_3$ film split-off, and annealing.

the surface of the thin film is smoothened by Ar$^+$ ion etching or mechanical polishing. The later can reduce the surface roughness below 1 nm rms.

Fig. 3a shows a photograph of a Z-cut LiNbO$_3$ thin film with dimensions of 12 mm × 10 mm × 600 nm bonded on a Cr-coated LiNbO$_3$ substrate. Such samples show good mechanical stability and chemical inertness needed for further
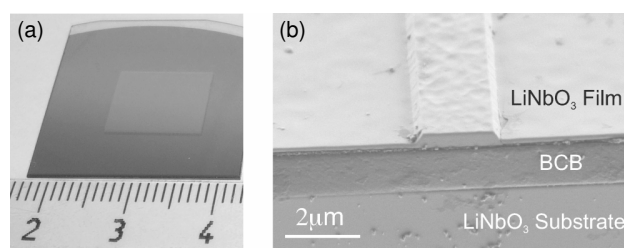
Figure 3 (a) Photograph of an ion-sliced LiNbO$_3$ thin film (12 mm × 10 mm × 600 nm) bonded on a Cr-coated LiNbO$_3$ substrate. (b) Polished edge of a LiNbO$_3$ thin film with a structured ridge waveguide for end-fire light coupling.
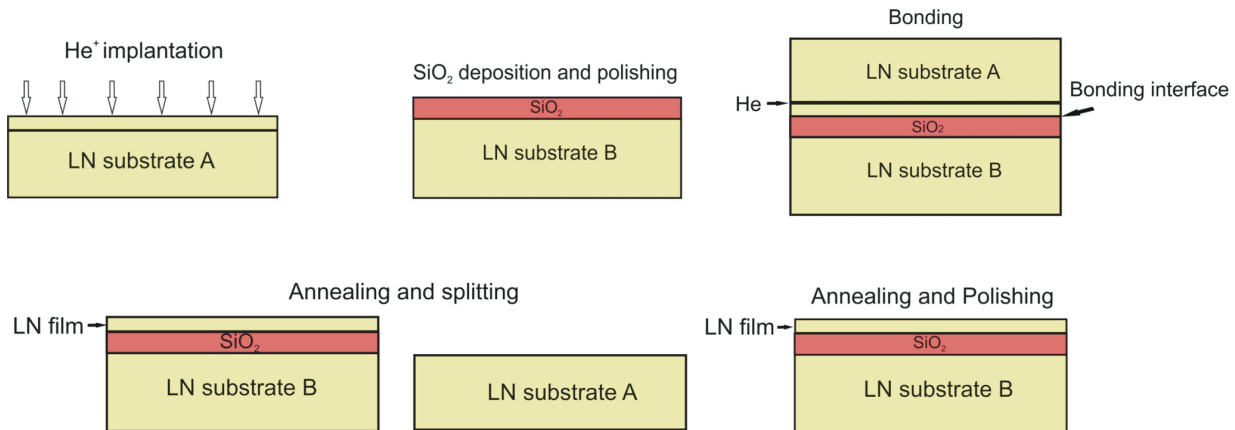
Figure 4 (online color at: www.lpr-journal.org) Fabrication scheme of LNOI: a "smart cut" single crystalline LiNbO$_3$ (LN) film of sub-micrometer thickness is crystal-bonded to a SiO$_2$ / LiNbO$_3$ (LN) substrate.

processing steps. Figure 3b shows a polished edge of a 200-nm thick LiNbO$_3$ film with a 600-nm high ridge waveguide for end-fire light coupling.

Single-crystalline LiNbO$_3$ films of this type were used as a platform for the first realization of electro-optically tunable microring resonators [16] which will be presented in Sect. 5. More recently, single-crystalline LiNbO$_3$ photonic crystal slabs were also fabricated and their optical properties were characterized [30] as described in Sect. 6.

2.3. Crystal bonding to SiO$_2$

To fabricate a LNOI structure, another choice of insulator is SiO$_2$ between the ion-sliced LiNbO$_3$ film and the substrate. In contrast to the BCB bonded material, annealing at much higher temperatures becomes possible. High temperature annealing can minimize ion-implantation induced material damage and helps to recover electro- and nonlinear optical properties. Moreover, it contributes significantly to a reduction of the surface roughness of LiNbO$_3$ ridge guides [31]. To avoid a thermal coefficient mismatch, the substrate should be LiNbO$_3$ bulk material as well.

A SiO$_2$ layer of high density is deposited on the LiNbO$_3$ substrate using plasma-enhanced chemical vapor deposition (PECVD), which also provides a very good adhesion. Moreover, the stress between SiO$_2$ and the LiNbO$_3$ substrate can be controlled by the parameters of the PECVD process. The SiO$_2$ surface roughness should be reduced by polishing to < 1 nm in order to enable a high bonding strength of ion-sliced LiNbO$_3$ film and SiO$_2$ layer.

Such directly bonded layer structures have been pioneered by the group of Günter [15] on smaller substrates. Recently, the Paderborn group succeeded in the fabrication of LNOI wafers of 3″ diameter [32] as described below.

2.4. Wafer scale fabrication of LNOI

In the following, the full-wafer process to fabricate LNOI is briefly described [17,32]. Also different sandwich structures

with a thin metal electrode either underneath the SiO$_2$ layer or underneath the LiNbO$_3$ film have been fabricated. Such structures should enable electric field induced poling and electro-optic control of light propagation. Even LNOI with a MgO:LiNbO$_3$ film on SiO$_2$ on a LiNbO$_3$ substrate has been demonstrated.

Full-wafer fabrication

The full wafer fabrication process is schematically shown in Fig. 4. At first, a Z-cut LiNbO$_3$ wafer of 3″ diameter is implanted by He-ions with a dose of 4×10^{16} ions/cm^2 forming an amorphous layer at a depth dependent on the implantation energy (see Fig. 1). Another Z-cut LiNbO$_3$ handle sample is coated by a SiO$_2$-layer of 1.3 µm thickness by plasma enhanced chemical vapor deposition (PECVD), and then annealed at 450 °C for 8 hours to drive off the gases trapped in the oxide layer. With a chemical mechanical polishing (CMP) process, the surface roughness is reduced from about 6 nm to 0.35 nm enabling direct wafer bonding (Fig. 5). The bonded pair of samples is then annealed (16 hrs. @ 165 °C + 6 hrs. @ 190 °C) to improve the bonding strength. By a further increase of the temperature (2 hrs. @ 228 °C), the sample splits along the He implanted layer. Afterwards, it is annealed at 450 °C for 8 hours, before the
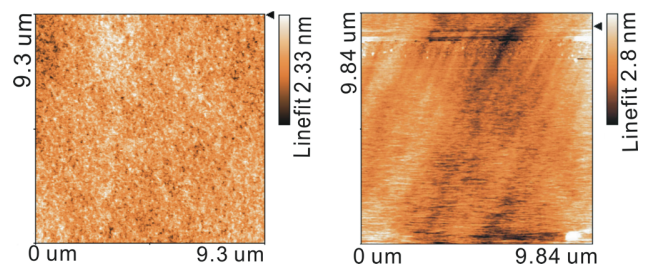
Figure 5 (online color at: www.lpr-journal.org) Left: AFM micrograph of a polished SiO$_2$ surface of RMS-roughness of 0.35 nm. Right: AFM micrograph of a polished LNOI surface of RMS-roughness of 0.5 nm.
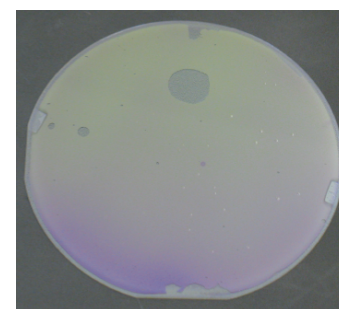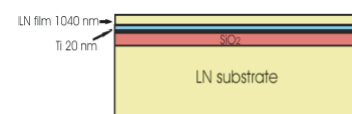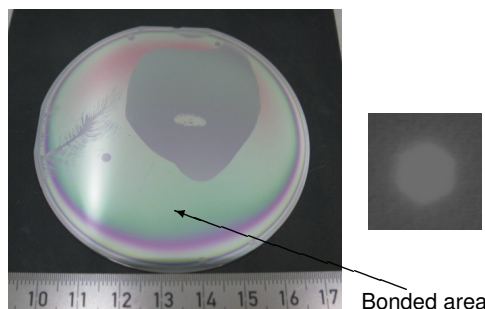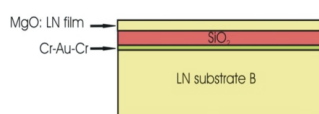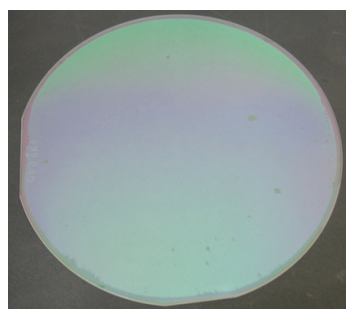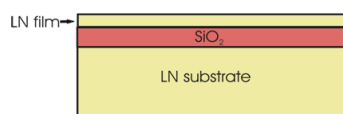
Figure 6 (online color at: www.lpr-journal.org) Schematic cross-section (top) and photograph (bottom) of a LNOI-wafer of 3″ diameter after splitting, consisting of a 760-nm thick single crystalline LiNbO$_3$ (LN) film crystal bonded on a 1.3-μm thick SiO$_2$ layer deposited by PECVD on a LiNbO$_3$ (LN) substrate.

Figure 7 (online color at: www.lpr-journal.org) Schematic cross-section (top) and photograph (bottom) of a LNOI wafer of 3″ diameter, consisting of a 1040-nm thick single crystalline MgO:LiNbO$_3$ (LN) film crystal bonded on a 1.3-μm thick SiO$_2$ layer deposited by PECVD on a thin ($\sim$40 nm) evaporated Cr-Au-Cr-electrode on a LiNbO$_3$ (LN) substrate. On the right: spontaneously formed micro-domain of inverted polarization after annealing at 450 °C for 5 hours. The size of the reversed domain is around 10 μm.

Figure 8 (online color at: www.lpr-journal.org) Schematic cross-section (top) and photograph (bottom) of a LNOI wafer of 3″ diameter, consisting of a 1040-nm thick single crystalline LiNbO$_3$ (LN) film crystal bonded on a 20-nm thick evaporated Ti electrode on a 1.3-μm thick SiO$_2$ layer deposited by PECVD on a LiNbO$_3$ (LN) substrate. The upper surface of the LiNbO$_3$ (LN) film is not yet polished after splitting.

LNOI-surface is polished to 0.5 nm roughness by another CMP-process (Fig. 5).

The CMP process and subsequent surface cleaning are of key importance to achieve the required high quality surfaces with lowest surface roughness and excellent flatness enabling direct wafer bonding. A scratch-free polished surface is obtained by filtering the polishing slurry. RCA cleaning is used to remove the particle contamination on the wafers.

LiNbO$_3$ film / SiO$_2$ / LiNbO$_3$ substrate

Fig. 6 presents a 3 inch LNOI wafer. The good homogeneity of the interference colors underlines the homogeneity of the fabrication process. A thickness variation within 6% is measured by a step profiler.

MgO:LiNbO$_3$ film / SiO$_2$ / Cr-Au-Cr / LiNbO$_3$ substrate

Fig. 7 shows the result of experiments to fabricate a LNOI wafer of 3 inch diameter with a MgO-doped LiNbO$_3$ thin film on top and a Cr-Au-Cr metal electrode underneath the SiO$_2$ layer. The idea was to take advantage of the lower coercive field of MgO:LiNbO$_3$ and to facilitate (light assisted) electric field poling via a second electrode on top of the LNOI surface. However, corresponding experiments failed up to now; it seems that the required conductivity of the SiO$_2$ layer is too low to allow the flow of the poling current. On the other hand, some spontaneously generated micro-domains could be observed after the final annealing and polishing processes (see Fig. 7).

LiNbO$_3$ film / Ti / SiO$_2$ / LiNbO$_3$ substrate

Also sandwich structures with a thin Ti-film as poling electrode on top of the SiO$_2$ layer have been developed (see Fig. 8). They are currently investigated to get electric field poling via a second electrode on top of the LNOI surface. Poling voltages of a few tens of Volts should be sufficient to overcome the coercive field.

A metal layer of Ti has been chosen to allow a thermal oxidation after poling. We expect that the resulting TiO$_2$ layer of high refractive index would only slightly modify the LNOI waveguide characteristics and would avoid ohmic losses for guided wave propagation. First experimental results are promising.

3. Micro- and Nanostructuring of LNOI

Due to their high index contrast of $\Delta n \approx 0.7$ ($n_{\text{LiNbO}_3} \approx 2.14$, $n_{\text{SiO}_2} \approx 1.44$), LNOI samples are strongly guiding planar waveguides even with sub-micrometer thickness of the core layer. As such they are ideally suited for the fabrication of LNOI photonic wires and micro-optical devices. However, their fabrication requires advanced micro- and nano-structuring methods including high resolution and flexible photolithography, chemical and ion beam etching techniques.

Two different types of optical lithography have been used to prepare photoresist masks enabling subsequent etching of the LiNbO$_3$ layer of LNOI; they are presented in Sect. 3.1. However, in contrast to SiO$_2$, LiNbO$_3$ is much harder to etch in such a way that smooth surfaces result,

a prerequisite for low loss waveguiding especially in optical channels of sub-micrometer dimensions. Chemical and ion beam etching techniques have been developed in the last years to fabricate high quality LiNbO$_3$ surfaces of low roughness [31, 33]. For the fabrication of LNOI photonic wires and micro-optical devices, inductively coupled plasma (ICP) etching was used resulting in high quality photonic wires (Sect. 3.2) and microring resonators (Sect. 3.3).

For sub-micrometer fabrication, focused ion beam (FIB) etching is a very precise and controllable method. It was used to drill photonic crystal structures into the LiNbO$_3$ layer of LNOI samples (Sect. 3.4).

For efficient quasi phase matched (QPM) nonlinear optical interactions in photonic wires, periodically poled (PP) structures are required. However, periodic poling of LNOI photonic wires proved to be a big challenge up to now. Therefore, an alternative strategy was used to develop first periodically poled LNOI samples, which were processed afterwards in the same way as mono-domain samples to fabricate periodically poled photonic wires (Sect. 3.5).

3.1. Standard optical and laser lithography

As shown in our previous studies [16, 17] (see also Sect. 4), LiNbO$_3$ channel waveguides embedded in BCB (n = 1.55) or crystal bonded on SiO$_2$ (n = 1.45) must be narrower than 1 µm in order to achieve single mode waveguiding at a wavelength of 1550 nm. Patterning of sub-micrometer wide waveguides and coupling gaps requires advanced techniques such as electron-beam- or laser-lithography or at least an electron-beam written mask for standard UV photolithography. While electron-beam lithography systems have higher resolution, laser writers can be more suitable for fast prototyping of integrated optical devices.

The Paderborn group used an electron-beam written mask of high precision to define photoresist stripes of 1–7 µm width and a thickness of 1.7 µm serving as etch masks. Due to the etching ratio of LiNbO$_3$ and photoresist of about 1.0, this relatively large thickness was necessary to enable an etching depth up to 460 nm by using inductively coupled plasma (ICP-)etching with Ar-ions (see also Sect. 3.2). Figure 9 schematically shows the cross-section of a LNOI sample with a photoresist mask before and after Ar-milling. A typical thickness of the LiNbO$_3$ layer was 730 nm crystal-bonded to a 1.3-µm thick SiO$_2$ layer on a Z-cut LiNbO$_3$ substrate. The CMP-polished surface had a rms-roughness of 0.5 nm.
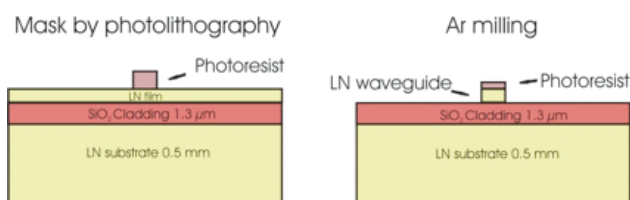
Figure 9 (online color at: www.lpr-journal.org) Schematic diagram of the cross-section of a LNOI sample (left) used to fabricate photonic wires by Ar-milling (right).
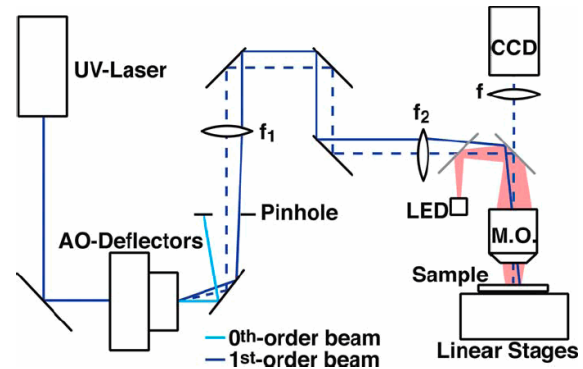

Figure 10 (online color at: www.lpr-journal.org) Scheme of the laser lithography system showing the main optical components and the laser beam path.

The Zürich group set up a compact laser lithography system operating at 375 nm wavelength, which is schematically shown in Fig. 10. The system consists of a continuous-wave, frequency stabilized diode laser, two acousto-optic deflectors (AOD) in series at right angles to give full two-dimensional scanning, a beam steering controller for driving the AODs, a microscope objective for focusing the laser beam, and three (xyz) motorized linear stages to position a sample. A CCD camera is used for observing the sample surface and for the positioning of the laser beam. Using a microscope objective with a high numerical aperture (NA > 0.75), sub-micrometer wide patterns can be written by the focused laser beam. The use of the AODs substantially enhances writing speed and precision needed for demanding structures. A detailed description of the laser lithography system and its performance can be found in [34].

### 3.2. Argon-milling (ICP-etching) of photonic wires

Using an Oxford Plasmalab System 100 the Paderborn group fabricated series of channel guides with dimensions down to sub-micrometer width and height. Ar-milling was used for typically 60 min with 100 W RF-power inductively coupled into the plasma (ICP) and 70 W RF power coupled to the sample table. The resulting etch depth was 460 nm. Figure 11 shows scanning electron micrographs (SEM) of a ridge guide of 1 µm top width. The dark stripe underneath is the SiO$_2$ layer on the LiNbO$_3$ substrate. On both sides of the ridge, etched trenches can be observed, resulting from additional etching by ions reflected by the angled walls of the ridge. Their slope of ∼ 27° (with respect to the vertical direction) is determined by the dependence of the etching rate on the incident angle of the ion beam. As the etched trenches apparently isolate the ridge, longer etching was not considered. However, it should be possible to completely remove the remaining LiNbO$_3$ layer by extending the etching time. Finally, the end faces of the sample were polished to enable efficient end-fire coupling of light. A typical sample length was 3 mm [17]. Results of a detailed characterization of these photonic wires are presented in Sect. 4.
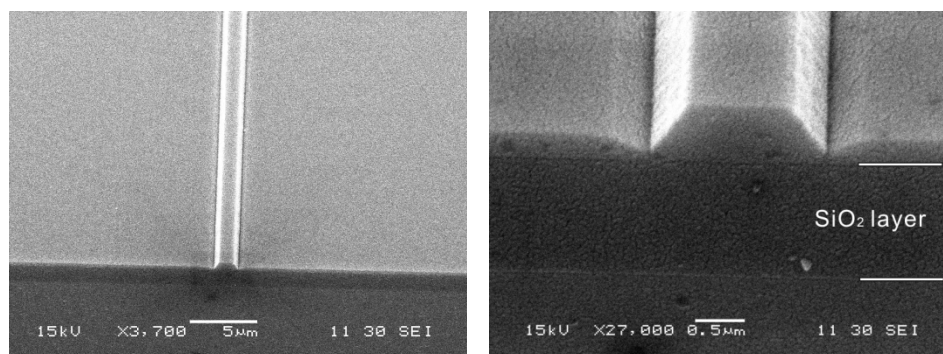
Figure 11 SEM micrographs of LNOI ridge guides (photonic wires) of sub-micrometer cross-section dimensions ($\sim 1\,\mu m$ top width). The trenches on both sides of the ridges nearly reach the surface of the SiO_2 buffer layer.

## 3.3. Argon-milling (ICP-etching) of photonic microrings and couplers

Using an Oxford Plasmalab 80+ the Zürich group fabricated micro-ring resonators with coupling waveguides. Figure 12a shows an example of a microring with a coupling waveguide, structured by the laser lithography system in a negative-tone photoresist film span on a $LiNbO_3$ crystal. To achieve 200-nm narrow coupling gaps, a double lithography process was used. In the first step, coupling waveguides were written in the photoresist film by moving the sample with the translation stages, and then the photoresist was developed and hardened. In the second step, the whole lithography process was repeated with a new photoresist film and the rings were written by precise steering of the laser beam using the acousto-optic deflectors. Figure 12b shows an example of a microring with a coupling waveguide on a $LiNbO_3$ crystal surface after Ar^+ ion etching. The etching depth is about 400 nm.
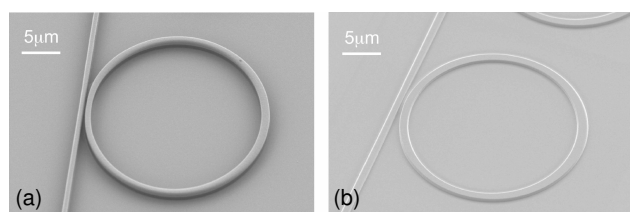
Figure 12 Scanning electron micrographs of a microring resonator with a coupling waveguide: (a) photoresist mask on a $LiNbO_3$ wafer written by the laser lithography system; (b) final structure transferred onto a $LiNbO_3$ crystal surface by Ar^+ ion ICP-etching (Ar-milling).

3.4. Focused ion beam milling

Fabrication of nanostructures such as arrays of cylindrical holes for photonic crystals requires even higher resolution. As shown in our previous study [30], focused ion beam (FIB) milling is very well suited for fast prototyping of high-quality cylindrical holes in ion-sliced $LiNbO_3$ thin films. In our experiments we used a Zeiss Nvision 40 device in combination with RAITH Elphy Quantum lithography system. Figure 13 shows a scanning electron micrograph
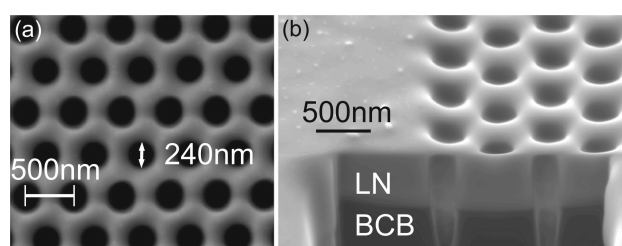

Figure 13 (a) Scanning electron micrograph of a triangular lattice of air holes in a Z-cut, 600-nm thick $LiNbO_3$ film milled by focused ion beam. The lattice constant is 500 nm and the air holes have a diameter of 240 nm. (b) Cross-section showing holes with a regular cylindrical shape in the $LiNbO_3$ thin film. The holes with a depth of 1 μm penetrate into the BCB underlayer.

of triangular lattice of air holes with a diameter of 240 nm and a lattice constant of 500 nm structured in a $LiNbO_3$ thin film. The holes were milled with a focused beam of Ga ions accelerated to 30 kV at a current of 300 pA. A single pass milling strategy was used which enables shorter processing times and is less prone to slight drifts of focused ion beam. In order to minimize unwanted charging effects during the ion beam milling, samples were covered with 5 to 10-nm thick chromium layer and electrically connected to the grounded sample holder. After the completion of the milling process, the chromium layer was removed by chemical etching. We note that the unwanted re-deposition effects in the milling process were minimized because of the relatively soft BCB underlayer, which facilitated the milling of cylindrical holes with vertical walls in $LiNbO_3$ thin films.

3.5. Periodically poled photonic wires

Up to now, direct electric field poling of LNOI samples or of photonic wires was not yet successful. We assume that small defects in the $LiNbO_3$ layer or in the $LiNbO_3$ channel lead to electrical breakdown before domain inversion is achieved. Therefore, we used an alternative strategy to develop periodically poled photonic wires as needed for QPM nonlinear optical interactions. Instead of starting with a single-domain $LiNbO_3$ substrate A (see Fig. 4) to fabricate a LNOI sample, a periodically poled substrate A was used and processed as described in Sect. 2.
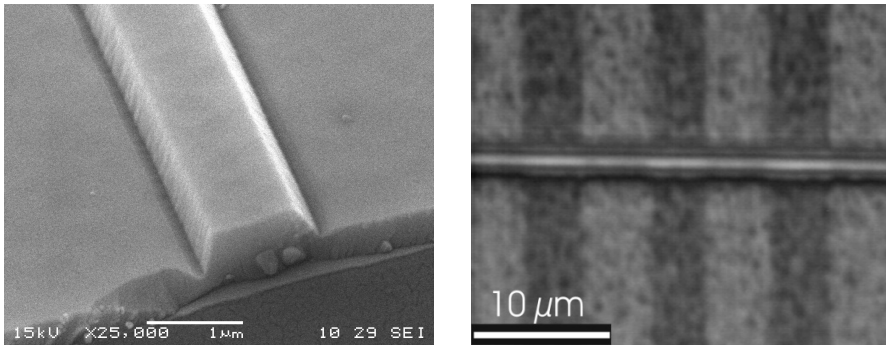
Figure 14 SEM micrograph (left) and optical micrograph (right) of a periodically poled LNOI photonic wire of 1 μm top width and 710 nm thickness. The periodicity of the ferroelectric domain grating is 9 μm.

The result was a periodically poled LNOI film. Also the definition and fabrication of channel guides using the PPLNOI film was done as discussed above for the single domain samples resulting in periodically poled LNOI photonic wires of 9 μm periodicity of the ferroelectric domain grating [35].

Figure 14 shows on the left a scanning electron microscope (SEM) micrograph of a PPLNOI photonic wire of 1 μm top width and 710 nm thickness. Again, on both sides of the ridge etched trenches can be observed, resulting from ions reflected by the angled walls of the ridge. As the domain structure was hardly visible in the SEM micrograph, also an optical micrograph was taken with a differential interference contrast microscope; it is shown on the right. The domain grating is clearly visible not only in the remaining $LiNbO_3$ film on both sides of the ridge, but also in the photonic wire itself.

4. Photonic wires

Photonic wires are important basic structures in integrated optics. They are channel waveguides of high index contrast and very small cross-section dimensions leading to strong light confinement. Due to their extremely small mode size, $LiNbO_3$ photonic wires are ideal candidates for efficient nonlinear optical devices. In particular, periodically poled structures would enable quasi phase matching (QPM) of second order nonlinear processes such as second harmonic generation (SHG), difference frequency generation (DFG), etc.

We have developed and carefully investigated several $LiNbO_3$ channels of sub-micrometer dimensions. Their fundamental optical properties were characterized around 1.55 μm wavelength. To be specific, their mode distributions were measured and compared with modeling results. The mode propagation losses were determined for different wire width and as function of the polarization using the resonator method [35]. A correct analysis required the knowledge of the waveguide end face reflectivity, which was evaluated for a number of parameters. Moreover, the resonator method allows determining the group index of the waveguides, which was measured in this way and also compared with modeling results [37]. Finally, (third order) quasi phase matched (QPM) second harmonic generation (SHG) was demonstrated in periodically poled LNOI photonic wires.

4.1. Coupling to photonic wires

A tunable laser diode was used to investigate the photonic wires. The light was coupled to the waveguides by a 60 ×/0.8 objective with an estimated coupling efficiency of about 40% (30%) to the fundamental mode of the wire of 2 (1) μm top width. On the output side, a 100 ×/0.9 objective magnified the near field distribution of the guided mode to form an image of maximum spatial resolution (~ 1.1 μm) measured by a camera.

4.2. Mode distributions

The mode distributions were measured as function of the waveguide width and of the polarization, and compared with simulated distributions calculated with a full-vectorial finite-difference method. According to the simulation results, both structures support not only the fundamental, but at least also the second order mode at 1.55 μm wavelength. However, by a careful adjustment of the input laser beam, the fundamental mode could be selectively excited. Moreover, the remaining thin $LiNbO_3$ films of 270 nm thickness on both sides of the photonic wires formed a planar waveguide for qTE polarization.

Figure 15 shows the measured mode distribution (a) for quasi TE-polarization (qTE) together with a corresponding
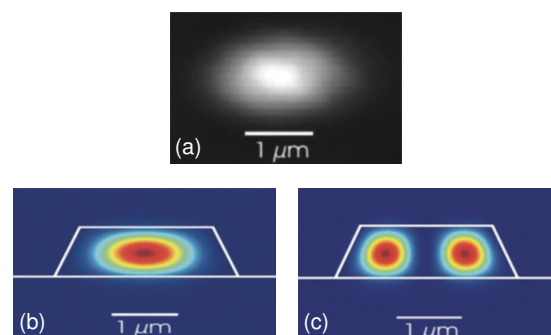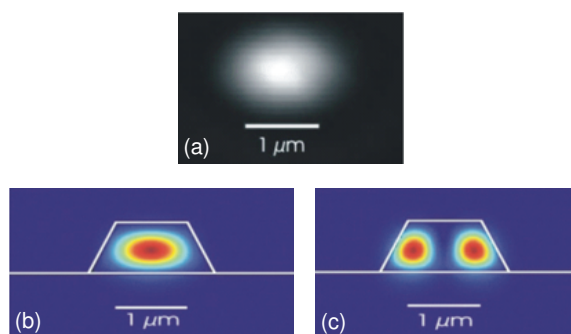

Figure 15 (online color at: www.lpr-journal.org) Measured (a) and calculated (b) intensity distribution of the fundamental mode in a photonic wire of 2 μm top width (qTE-polarization; $\lambda = 1.55$ μm). The intensity distribution of the simulated second order mode is shown in (c). The profile of the ridge, used for the simulations, is indicated (b,c).

modeling result (b) at the output of a 2-µm wide photonic wire. In view of the finite spatial resolution of the imaging system, the agreement is reasonable. The calculated second order mode is displayed in Fig. 15c.

Fig. 16 shows the measured (a) and calculated (b) distribution of the fundamental quasi TM mode (qTM) in a photonic wire of 1 µm top width. Again, in view of the finite spatial resolution of the imaging system, the agreement is reasonable. The intensity distribution of the simulated second order mode is shown in Fig. 16c.


Figure 16 (online color at: www.lpr-journal.org) Measured (a) and calculated (b) intensity distribution of the fundamental mode in a channel waveguide of 1 µm top width (qTM-polarization; $\lambda = 1.55$ µm). The intensity distribution of the simulated second order mode is shown in (c). The profile of the ridge, used for the simulations, is indicated (b,c).

The cross-section of the fundamental mode of the 1 µm wide photonic wire is about 0.4 µm^2 (product of FWHM in horizontal and vertical directions of the calculated distribution), more than one order of magnitude smaller than the mode size of about 16 µm^2 in a conventional Ti-indiffused strip guide of 7 µm width. Therefore, such photonic wires are ideal candidates to develop nonlinear devices of high efficiency. Moreover, high bending radii become possible without inducing excess bending losses.

4.3. End face reflectivities

Due to the small waveguide cross-section, the modal reflectivity R (ratio of reflected mode power to the incident mode power) can no longer be approximated by the Fresnel result for plane waves of normal incidence at a LiNbO$_3$ / air
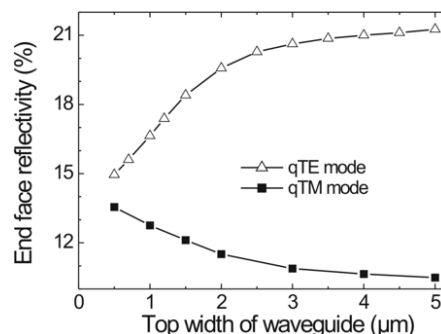

Figure 17 Calculated end face reflectivities of the fundamental modes of qTE and qTM polarization, respectively, versus the top width of LiNbO$_3$ photonic wires of 730 nm thickness.

interface ($\sim 14\%$) as usually done for weakly guiding structures. The actual value of R is needed to enable a correct evaluation of the propagation losses by using the resonator method [36] (see also next subsection). Therefore, R was calculated by a 3-dimensional finite difference time domain (FDTD) solver [38]. The result is presented in Fig. 17 as function of the top width of the ridge guides of 730 nm thickness. The slope of the ridges was kept constant assuming an angle of 27° with respect to the normal on the waveguide substrate. With increasing waveguide width, the end face reflectivity R approaches polarization dependent limits with a significantly higher reflectivity for qTE than for qTM modes. Due to the small waveguide thickness of 730 nm only, the reflectivity difference $\Delta R = R_{qTE} - R_{qTM}$ converges to $\sim 11\%$. This figure shrinks to $\sim 1\%$ with increasing thickness, determined by the birefringence of LiNbO$_3$ alone. With decreasing waveguide width (at 730 nm thickness), ΔR also shrinks to small figures, as qTE and qTM modes become nearly degenerate.

4.4. Propagation losses

The polished waveguide end faces of reflectivity R, as calculated above, form low-finesse waveguide cavities. By analyzing the contrast K of the cavity resonances, measured as function of the wavelength, the mode propagation losses were determined. This method is independent on the mode excitation efficiency [36].

Figure 18 shows two examples: on the left, the measured normalized transmission of a channel guide (photonic wire)
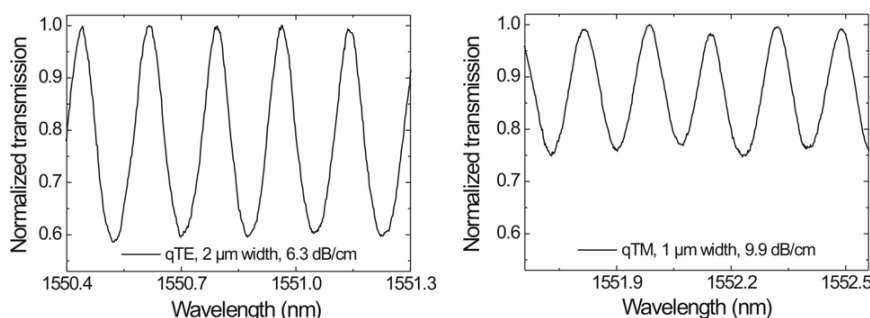
Figure 18 Normalized transmission of a channel guide of 2 (1) µm top width for qTE (qTM) polarization as function of the wavelength (left/right).

of 2 µm top width for qTE polarization as function of the
wavelength is presented; on the right, the transmission of
a channel guide of 1 µm top width for qTM polarization is
shown. A qTE-propagation loss of 6.3 dB/cm was evaluated
for the 2-µm wide channel; for qTM polarization, the loss
is 7.5 dB/cm. In the 1-µm wide photonic wire the qTM
propagation loss was determined to be 9.9 dB/cm; for qTE
polarization, the loss is 12.9 dB/cm. The larger qTE losses
in the narrower wire may result from some light coupling
to the thin planar (single polarization) waveguides on both
sides of the channel.

The losses very likely arise from scattering by the resid-
ual roughness of all four walls of the ridge. Losses due to a
coupling of the propagating light across the SiO$_2$ layer to
the substrate should be negligible (< 0.05 dB/cm), accord-
ing to the calculations with a fully vectorial finite difference
mode solver.

4.5. Effective and group indices

The waveguide mode dispersion is determined by the mate-
rial dispersion of core and cladding materials and also by the
waveguide dimensions [39]. Due to the high index contrast
of the photonic wires and their small cross-section dimen-
sions, the effective index of refraction n_{eff} varies consider-
ably as function of the wavelength. It was calculated by the
finite difference method for the fundamental qTE- and qTM-
modes [40], respectively, and for several waveguide widths
and wavelengths; some results are displayed in Fig. 19 to-
gether with the dispersion of bulk LiNbO$_3$ and SiO$_2$.

Whereas the effective mode index n_{eff} is difficult to
measure, the group index n_g could be derived in a small
wavelength range from the measured transmission spectra
of the waveguides (see Fig. 18): $n_g = \lambda^2/(2 \cdot L \cdot \Delta\lambda)$; L is
the waveguide length and $\Delta\lambda$ is the wavelength difference of
neighboring resonances [39, 41, 42]. In addition, the group
index was also calculated as $n_g = n_{eff} - \lambda \cdot (dn_{eff}/d\lambda)$; mea-
sured and calculated results are shown in Fig. 19 for the
fundamental modes of qTE and qTM polarization, respec-

tively. For comparison, also the calculated group index of
bulk LiNbO$_3$ is shown derived from a Sellmeier equation
describing the dispersion of bulk LiNbO$_3$ [43].

The effective indices of refraction vary between the bulk
indices of LiNbO$_3$ and SiO$_2$; the longer the wavelength and
the smaller the waveguides' cross sections are, the lower
the effective indices become due to a decreasing mode con-
finement. At shorter wavelengths, the mode is more and
more confined in the LiNbO$_3$ core of the waveguide and
n_{eff} approaches the (polarization dependent) bulk index of
LiNbO$_3$. The group indices for light propagation in the pho-
tonic wires are substantially larger than for light propagation
in bulk LiNbO$_3$, reflecting the influence of the small wave-
guide dimensions. They even allow adjusting a group index
dispersion close to zero in the 1.5 µm wavelength range,
which is of interest for optical communication devices.

4.6. Quasi phase matched (QPM) SHG in periodically poled photonic wires

Due to the modified dispersion in the nonlinear LNOI pho-
tonic wires, also their phase matching properties for non-
linear interactions are correspondingly dependent on the
waveguide dimensions [44]. They were theoretically inves-
tigated for second harmonic generation (SHG) taking also
periodically poled domain gratings into account to get quasi
phase matched (QPM) interactions. For periodically poled
(PP)LNOI photonic wires, the calculations showed that type
I QPM SHG for a fundamental wave of 1064 nm wave-
length should be possible in a wire of 1 µm top width and
730 nm thickness with a domain grating of 3 µm periodicity.
As such a small periodicity has not yet been fabricated, the
third order QPM SHG was considered via the corresponding
Fourier component of the 9 µm grating already developed
(see Fig. 14). This process should be possible at the expense
of a reduced efficiency. Figure 20 (left) shows the simulated
normalized SHG characteristics (for 3 µm periodicity) for
different lengths of the grating; the shorter the nonlinear
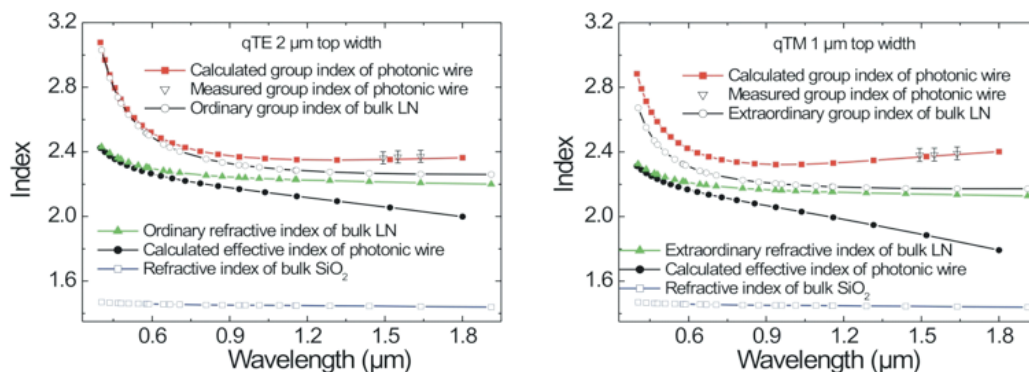
Figure 19 (online color at: www.lpr-journal.org) Calculated effective and group indices for the fundamental modes of qTE and qTM
polarization in photonic wires of 730 nm thickness and of 2 µm and 1 µm top width, respectively, versus the wavelength. The measured
group indices of photonic wires, the calculated group indices of bulk LiNbO$_3$ (LN), and the refractive indices of bulk LiNbO$_3$ and SiO$_2$
are shown as well for comparison.
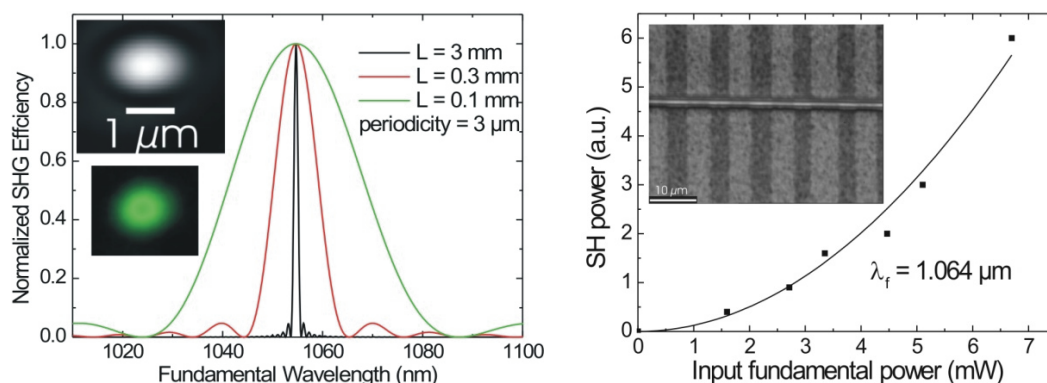
Figure 20 (online color at: www.lpr-journal.org) Left: Calculated (first order) quasi phase matching characteristics for SHG with different (interaction) lengths L. Upper and lower insets: photographs of TM-polarized modes of the fundamental (λ = 1064 nm) and the SH mode (λ = 532 nm), respectively. Right: measured (dots) and theoretical (fitted parabola, solid line) SH power versus input fundamental power (measured in front of the coupling lens). Inset: optical micrograph of a PPLN photonic wire of 1 µm top width and 9.0 µm periodicity.

interaction length, the broader the phase matching characteristic is. As only a section of ~ 100 µm length of the 3 mm long waveguide was successfully poled, uncritical phase matching was expected.

To test SHG in the PPLNOI photonic wires, light of 1064 nm wavelength from a narrow-band laser diode of up to 40 mW output power was coupled to a waveguide. The SH output power was detected by a photomultiplier which is sensitive at the SH and blind at the fundamental wavelength. The insets of Fig. 20 (left) show the observed modes of a photonic wire of 1 µm top width and 710 nm thickness at 1064 nm and 532 nm wavelength, respectively. Due to the broad phase matching characteristics, SHG could also be observed in waveguides of 2–7 width. The dependence of the generated SH power on the input fundamental power is shown in Fig. 20 (right); as expected, a parabolic dependence is observed.

5. Microring Resonators

Optical microring resonators are considered to be one of the main building blocks in future very-large-scale integrated photonic devices. We have realized two different types of LiNbO$_3$ microring resonators. Microrings of the first type are obtained by planar structuring of BCB-bonded LNOI samples and are thus suitable for high-density integration on a single chip. The second types are free-standing LiNbO$_3$ microrings which can be transferred onto any arbitrary host substrate to build hybrid integrated optics devices.

5.1. Microring resonators in LiNbO$_3$ thin films

Fig. 21 shows a schematic cross-section of the first electro-optically tunable microring resonators realized in Z-cut LiNbO$_3$ thin films [16]. The microrings are covered with a SiO$_2$ cladding and upper Cr electrodes. This configuration allows the applied electric field to be along the Z-axis of
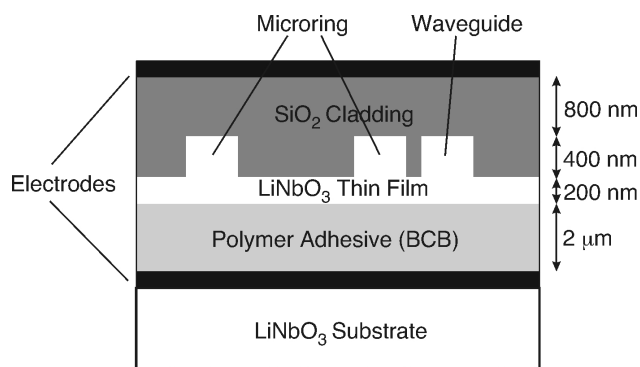

Figure 21 Schematic cross-section of an electro-optically tunable microring resonator based on BCB-bonded LNOI.

LiNbO$_3$ and therefore exploits the largest electro-optic coefficient r$_{33}$. It also enables to realize complex devices with separate upper electrodes for the independent control of different electro-optical microring resonators on a single chip.

Initially, the quality of these microring resonators was limited mainly by the lithography process performed by a standard mask aligner. Therefore, the minimum radius of useful microrings was limited to 100 µm, yielding a free spectral range (FSR) of 1.7 nm. Figure 22 shows an example of a transmission spectrum for TM polarized light and a shift of the resonance dip at 1555 nm upon applying 100 VDC on the electrodes. A shift of 0.11 nm corresponds to a tunability of 0.14 GHz/V. An increase of the tunability is feasible by reducing the thickness of cladding layers (SiO$_2$ and BCB) and by using semi-transparent electrodes.

Using the recently developed laser lithography system [34], optical waveguides with better surface quality were obtained, allowing smaller curvature radii. Figure 23 shows a scanning electron micrograph of a racetrack microring resonator with a curvature radius of 20 µm and a 10-µm long coupling region with a gap of 200 nm. From the transmission measurements a FSR of 7 nm and a quality factor Q of around 10,000 were deduced.
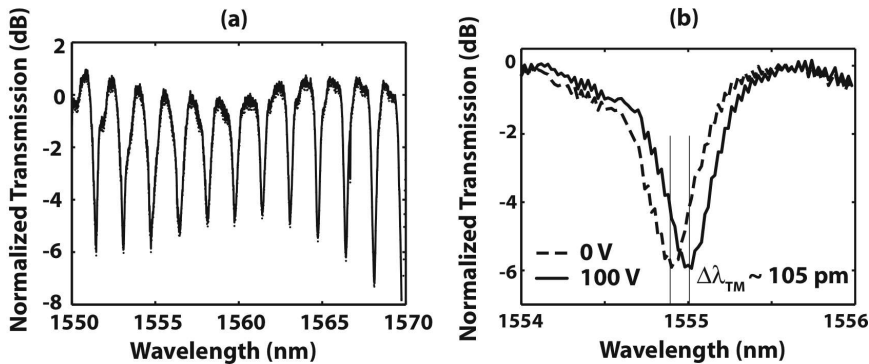
Figure 22 (a) Measured transmission (TM polarization) at the through port of a LiNbO$_3$ microring with a radius of 100 μm structured using a mask aligner. (b) Resonance dip at a wavelength of 1555 nm (dashed line) and the corresponding electro-optically shifted curve (solid line) upon applying 100 VDC to the device electrodes.
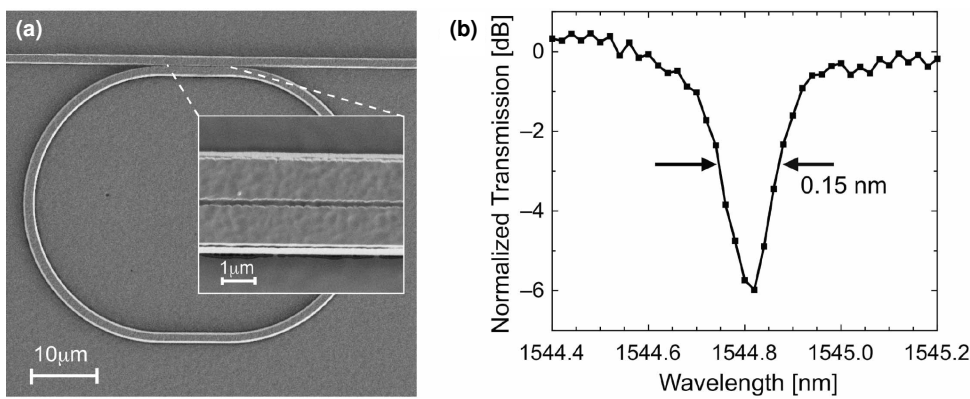

Figure 23 (a) Racetrack microring resonator in a LiNbO$_3$ thin film structured by laser lithography patterning and Ar$^+$ ion etching. (b) Transmission resonance dip with a width of 0.15 nm (FWHM) at a wavelength of 1544.8 nm

5.2. Free-standing microrings for hybrid integration

Further design and functional versatility of microring resonators can be achieved by combining different materials for coupling waveguides and microrings, such as semiconductors, glass-compounds, polymers and organic epitaxial layers. For this purposes we developed a novel technique, which enables the fabrication of free-standing microrings from BCB-bonded LNOI. The structuring procedure is the same as described above; however, the rings are etched completely down to the BCB layer. A sample with isolated microrings is then put into a bath of standard clean-1 (SC-1) solution at a temperature of 100 °C. In this step, the adhesion between the LiNbO$_3$ microrings and the BCB layer is strongly reduced. The microrings remaining on the top of the substrate become freely movable and can be transferred onto any arbitrary host substrate where they can be positioned with submicrometer accuracy using micropositioning tools or other alignment techniques.

Based on this approach we realized for the first time LiNbO$_3$ microrings vertically coupled to gallium nitride (GaN) coupling waveguides on a sapphire substrate [45]. GaN exhibits low absorption in the near infrared wavelength range and a refractive index matching that of LiNbO$_3$. Figure 24 shows a scanning electron micrograph of a free-standing LiNbO$_3$ microresonator with a radius of 20 μm, which was positioned on a GaN waveguide.

In order to optimize the vertical light coupling, a sapphire substrate with GaN waveguides was first covered with a 100-nm thick layer of silicon nitride (PECVD at 300 °C).
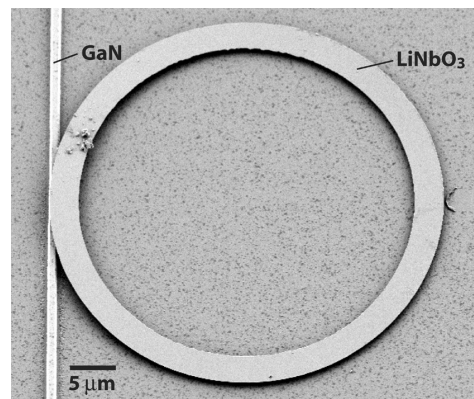
Figure 24 Scanning electron micrograph of a free-standing LiNbO$_3$ microring with a radius of 20 μm, positioned on a straight GaN waveguide. Below is a sapphire wafer used as a substrate. The widths of the coupling waveguide and of the microring are 1.1 μm and 3.0 μm, respectively. Both structures have a height of 600 nm.

Subsequently, free-standing LiNbO$_3$ microrings were transferred and aligned on top of the GaN waveguides. Finally, a thin cladding layer of SiN was deposited to fix the microrings at the aligned positions. A TE-polarized transmission spectrum of such a microring resonator is shown in Fig. 25. It exhibits sharp resonance dips with a linewidth of 0.15 nm FWHM and an extinction ratio of up to 18 dB, separated by a FSR = 7.9 nm at 1.55 μm.
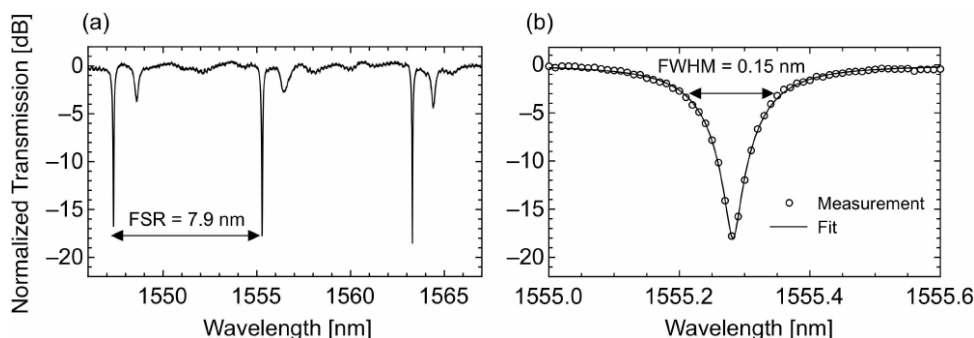
Figure 25 (a) Measured transmission spectrum (TE-polarization) through a GaN port waveguide of a free-standing $LiNbO_3$ microring resonator. (b) Detail of the measured resonance dip at 1555.28 nm with a linewidth of 0.15 nm FWHM and an extinction ratio of 18 dB.

From these measured values we deduced a finesse of 53 and quality factor $Q \sim 10,000$. From the fit of the measured resonance dip shown in Fig. 25b we estimated the total propagation losses of 17 dB/cm for the zero-order TE mode in the $LiNbO_3$ microring. The rather wide microring (2.5 μm) obviously supported also higher order modes as well, which are manifested in broader shallow dips between the sharp resonances.
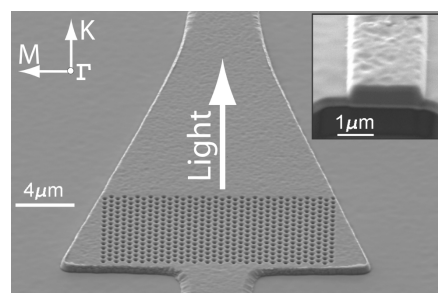
6. Photonic Crystal Slabs

Photonic crystal (PhC) structures have a great potential to reduce the size and increase the functionality of integrated optics devices. Up to now, a remarkable progress in the realization of high quality PhC structures has been achieved mainly in silicon and some other semiconductor materials. PhC structures in $LiNbO_3$ are of great interest because they offer a possibility to build very small electro-optical modulators and switches. In the past, most of the studies on PhCs in $LiNbO_3$ have been performed using annealed proton exchanged waveguides with weak optical guiding [46–49]. However, the development of high-quality PhC structures requires single-crystalline $LiNbO_3$ slabs, which provide strong index guiding in the vertical direction. In the following we describe first PhC structures realized in BCB-bonded LNOI samples [30].

Using the FIB milling as described in Sect. 3.4, we fabricated various triangular photonic crystal lattices with different number of holes in the middle of ridge optical waveguides to facilitate the in- and out-coupling of probe laser light. Figure 26 shows an example of a ridge optical waveguide with a tapered section containing a triangular array of 15 × 36 air holes (lattice period = 500 nm, hole diameter = 240 nm). The tapered waveguide structure was chosen to recollect the diffracted light passing through the photonic crystal lattice. The fabricated sample with a length of 3 mm contained several parallel optical waveguides with and without photonic crystal structures for comparative transmission measurements. The total milling time for the shown array of holes amounted to around 6 min. Thus, focused ion beam milling is a very suitable method for fast prototyping of high-quality photonic crystal structures in LNOI.

In order to experimentally demonstrate the existence of photonic bandgaps in the fabricated structures we performed optical transmission measurements. An optical setup for the transmission measurements is shown in Fig. 27. It consists mainly of a white light laser source, beam focusing and collimating optics, and a spectrometer (ANDO AQ-6315A) to analyze the transmitted spectrum. The laser source was a commercially available supercontinuum fiber laser (Fianium SC450) delivering 2 W of average output power within a broad spectral range between 450 and 1950 nm. Two rotatable Glan-Taylor polarizers were used to adjust the polarization and power of the in-coupled light.

Fig. 28 depicts a measured normalized transmission spectrum (full line) of the triangular lattice shown in Fig. 26. The measurements were performed with TE-polarized light

Figure 26 Scanning electron micrograph of a ridge optical waveguide with a tapered region containing a triangular photonic crystal lattice of 15 × 36 air holes. Light is propagating along symmetry direction $\Gamma \rightarrow K$. The inset shows an input facet of the coupling optical waveguide smoothened by FIB milling.
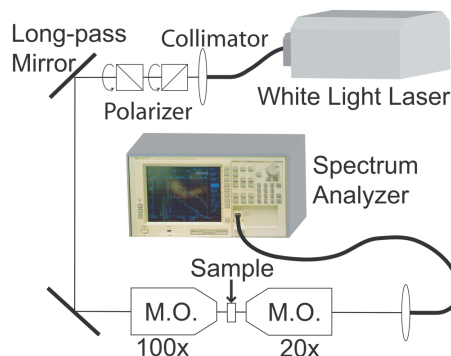
Figure 27 (online color at: www.lpr-journal.org) Optical set-up with a white light laser source and a spectrum analyzer for the characterization of the fabricated photonic crystal structures.
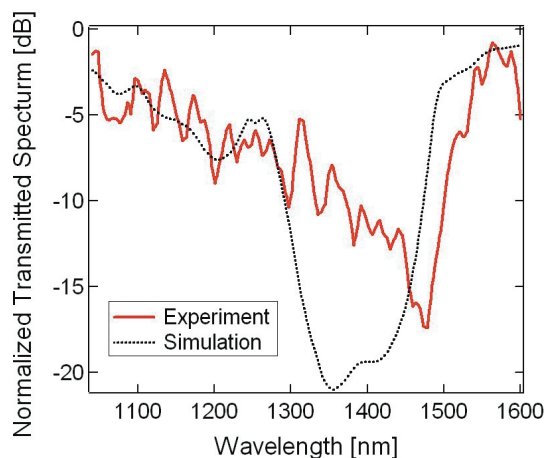
Figure 28 (online color at: www.lpr-journal.org) Measured (solid line) and calculated (dotted line) normalized transmission through the photonic crystal structure shown in Fig. 26.

(polarization parallel to the LNOI surface) over the wavelength range from 1050 to 1600 nm. The normalized transmission spectrum was obtained by dividing two transmission spectra of adjacent waveguides with and without a photonic crystal structure in the middle. As it can be seen, the spectrum shows a broad dip between 1300 and 1500 nm with the maximum extinction ratio of 15 dB at a wavelength of 1470 nm. In contrast to the TE polarization, no photonic gap was observed for TM polarized light, which is in accordance with a theoretical analysis of the fabricated structure. Although the fabricated slabs are not symmetric in the vertical direction (air/ LiNbO$_3$/BCB), the band gap effects are still possible due to strong confinement of propagation modes in the vertical direction [50]. The transmission properties of the fabricated structure were also modeled using a three-dimensional finite-difference time-domain software (OptiFDTD, Optiwave Systems Inc.). Figure 28 shows a comparison of the calculated transmission (dotted line) and the measured transmission (solid line). We contribute the deviations between both curves to differences between the designed (ideal) and fabricated structure.

7. Conclusions and Perspectives

The recent development of high-index contrast "lithium niobate on insulator" (LNOI) has been reviewed. Submicrometer thin single-crystalline LiNbO$_3$ films, bonded to a low-index substrate, are obtained by "ion-slicing" with He$^+$-ions of ~ 200 keV energy. Two complementary techniques for bonding have been developed. Benzocyclobutene (BCB), which simultaneously serves as low-index cladding layer, enables relatively easy bonding to a LiNbO$_3$ substrate. On the other hand, crystal bonding – exploiting van der Waals forces – on a vacuum deposited SiO$_2$-layer on a LiNbO$_3$ substrate allows high annealing temperatures, important to reduce ion-implantation induced material damage and to recover electro- and nonlinear optical properties of the LiNbO$_3$ waveguide layer. A full wafer (3$''$ diameter)

technology has been developed to fabricate LNOI of different material and layer compositions. Even periodically poled LNOI could be fabricated in this way.

Similar to SOI (silicon-on-insulator) LNOI might become a new platform for high-density integrated optics. It has – in contrast to SOI – excellent electro-optic, acousto-optic, and nonlinear optical properties. Moreover, it can be easily doped with rare-earth ions to get a laser active material. Therefore, several micro- and nano-structuring techniques, such as conventional and laser beam lithography of high resolution, chemical etching and (focused) ion-beam milling and focused ion-beam etching, have been used to develop a number of micro-photonic devices.

As basic structures, LNOI photonic wires with cross-section $< 1\,\mu m^2$ have been developed. Their most interesting dispersion properties can be adjusted by the waveguide dimensions alone in a wide range. Also periodically poled (PP)LNOI photonic wires have been fabricated with a domain period of 9 μm and second harmonic generation (SHG) could be successfully demonstrated. Due to their small mode size, PPLNOI photonic wires have a great potential for the development of second order nonlinear devices of unprecedented efficiency. They are ideal candidates for the development of a wide range of nonlinear wavelength converters and of devices for all-optical signal processing. In particular, sub-micrometer ferroelectric domain structures would be very attractive enabling devices with backward nonlinear coupling.

Using a high-resolution laser lithography system, electro-optically tunable LNOI microring resonators with a waveguide curvature of 20 μm and a footprint of $45 \times 55\,\mu m^2$ only have been developed. Their high quality is demonstrated by a Q-value up to 10,000. A tunability of 0.14 GHz/V could be shown. Moreover, free standing LiNbO$_3$ micro-rings of 20 μm radius have been developed for hybrid integration with nearly arbitrary materials; this is demonstrated by vertical coupling to a GaN channel guide on a sapphire substrate. A finesse of 53 and a free spectral range of 7.9 nm at 1.55 μm wavelength have been obtained.

Photonic crystal structures have been fabricated based on BCB-bonded LNOI. Both, simulation and experimental results show a photonic bandgap around 1470 nm wavelength, a first step towards the realization of electro-optically tunable photonic bandgap structures.

The growing activities and the great potential of LNOI based devices will lead to novel concepts and architectures of a high-density integrated optics with highly efficient electro-optical, nonlinear-optical, and laser/amplifier devices.

Gorazd Poberaj received the B. Sc., M. Sc., and Ph. D. degree in physics from the University of Ljubljana, Slovenia, in 1993, 1997, and 2000, respectively. From 1993 to 1995 he worked as R&D engineer in the Laser Division of Fotona d.d Company, Ljubljana, Slovenia. From 1996 to 1997 he was a visiting scientist at the Institute of Technical Physics of the German Aerospace Center (DLR) in Stuttgart. In 1998 he joined the Institute of Atmospheric Physics at the German Aerospace Center in Oberpfaffenhofen, where he performed his Ph. D. and post-doctoral research work. From 2004 to 2010 he was senior scientist and project leader in the Nonlinear Optics Laboratory at the Swiss Federal Institute of Technology (ETH), Zurich. His main research fields were integrated optics, nonlinear optics, and tunable THz generation. Since August 2010 he is with the laser company Onefive GmbH in Zurich, Switzerland, working as R&D project manager in the field of ultrafast lasers for industrial and scientific applications.

Hui Hu received the B. S. and Ph. D. degrees in physics from Shandong University, Jinan, China, in 1996 and 2001, respectively. From 2001 to 2003, he was with the Electronic Engineering Department, Tsinghua University, China, working on MOCVD growth of Group III-Nitrides. From 2004 to 2010, he was with the Physics Department, University of Paderborn, Germany, as an Alexander von Humboldt (AvH) Research Fellow and post-doc, working on lithium niobate integrated optics. He is currently a professor at Physics School, Shandong University, China. His research interests include micro-fabrication and integrated optics.

Peter Günter is emeritus professor of physics at the Swiss Federal Institute of Technology (ETH). He performed his studies at ETH and obtained the master degree (dipl. Phys. ETH) in 1971 and the Ph. D. in Physics in 1976. In 1982 he became senior lecturer and from 1986–2008 he was professor of experimental physics and head of the Nonlinear Optics Laboratory at ETH. He was a visiting professor at Stanford University, at the Université Paris-Sud, a Distinguished Visiting Lecturer at the Center for Research in Electro-Optics and Lasers (CREOL), and a visiting scientist at the Institute for Physical and Chemical Research (RIKEN), the Georgia Institute of Technology and the University of Washington. Since 1971 he has been engaged in research on electro-optics, nonlinear optics, integrated optics and optical microresonators, photorefractive phenomena in organic and inorganic materials, terahertz generation.

Wolfgang Sohler received the diploma and Dr. rer. nat. degrees in physics from the University of Munich, Germany, in 1970 and 1974, respectively. From 1975 to 1980 he was with the University of Dortmund, Germany, working on integrated optics. In 1980 he joined the Fraunhofer Institut für Physikalische Messtechnik, Freiburg, Germany, as head of the Department of Fibre Optics. Since 1982 he has been with the University of Paderborn, Germany, as Professor of Applied Physics. His research interests include integrated optics, fibre optics and laser physics. He is the (co-)author of more than 250 journal and conference contributions and of several book chapters. In 2001 he was organizer and conference chairman of the 10th European Conference on Integrated Optics (ECIO '01) in Paderborn.

References

[1] G. T. Reed, Nature **427**, 595–596 (2004).

[2] R. U. Ahmad, F. Pizzuto, G. S. Camarda, R. L. Espinola, H. Rao, and R. M. Osgood, IEEE Phot. Tech. Lett. 14, 65–67 (2002).

[3] Y. A. Vlasov and S. J. McNab, Opt. Express **12**, 1622–1631 (2004).

[4] Y. Kokubun, IEICE Trans. Electron. **E90-C**(5), 1037–1045 (2007).

[5] B. S. Song, S. Noda, T. Asano, Y. Akahane, Nature Mat. **4**, 207–210 (2005).

[6] W. Sohler, B. Das, D. Dey, S. Reza, H. Suche, R. Ricken, IEICE Trans. Electron. **E88-C**(5), 990–997 (2005).

[7] Y. Sakashita, H. J. Segawa, Appl. Phys. 77, 5995–5999 (1995).

[8] X. Lansiaux, E. Dogheche, D. Remiens, M. Guillouxviry, A. Perrin, P. Ruterana, J. Appl. Phys. **90**, 5274–5277 (2001).

[9] F. Gitmans, Z. Sitar, and P. Günter, Vacuum **46**, 939–942 (1995).

[10] J. G. Yoon, K. Kim, Appl. Phys. Lett. 68, 2523–2525 (1996).

[11] Y. Nakata, S. Gunji, T. Okada, M. Maeda, Appl. Phys. A **79**, 1279–1282 (2004).

[12] M. Bruel, Mater. Res. Soc. Bull. **23**(12), 35–39 (1998).

[13] M. Bruel, Electron Lett. 31, 1201–1202 (1995).

[14] D. Djukic, G. Cerda-Pons, R. M. Roth, R. M. Osgood, S. Bakhru, and H. Bakhru, Appl. Phys. Lett. **90**, 171116 (2007).

[15] P. Rabiei and P. Günter, Appl. Phys. Lett. 85, 4603–4605 (2004).

[16] A. Guarino, G. Poberaj, D. Rezzonico, R. Degl'Innocenti, P. Günter, Nature Photonics **1**, 407–410 (2007).

[17] H. Hu, R. Ricken, and W. Sohler, in: Proceedings of the Topical Meeting "Photorefractive Materials, Effects, and Devices – Control of Light and Matter" (PR'09), Bad Honnef, Germany, 2009.

[18] T. A. Ramadan, M. Levy, R. M. Osgood, Appl. Phys. Lett. **76**, 1407–1409 (2000).

[19] R. M. Roth, D. Djukic, Y. S. Lee, R. M. Osgood, S. Bakhru, B. Laulicht, K. Dunn, H. Bakhru, L. Wu, and M. Huang, Appl. Phys. Lett. **89**, 112906 (2006).

[20] M. Levy, R. M. Osgood, Jr., R. Liu, L. E. Cross, G. S. Cargill III, A. Kumar, and H. Bakhru, Appl. Phys. Lett. **73**, 2293–2295 (1998).

[21] I. Szafraniak, I. Radu, R. Scholz, M. Alexe, and U. Gösele, Integrated Ferroelectrics **55**, 983–990 (2003).

[22] P. Rabiei and W. H. Steier, Appl. Phys. Lett. **86**(16), 161115 (2005).

[23] K. Diest, M. J. Archer, J. A. Dionne, Y.-B. Park, M. J. Czubakowski, and H. A. Atwater, Appl. Phys. Lett. **93**, 092906 (2008).

[24] M. Levy and A. M. Radojevic, in: Wafer Bonding: Applications and Technology, edited by M. Alexe and U. Gösele, Springer Series in Material Sciences (Springer, Berlin, Heidelberg, 2004), pp 417–450.

[25] A. M. Radojevic, M. Levy, J. R. M. Osgood, A. Kumar, H. Bakhru, C. Tian, C. Evans, Appl. Phys. Lett. **74**, 3197–3199 (1999).

[26] http://www.srim.org, date of last visit: 7 February 2012.

[27] D. Burdeaux, P. Townsend, J. Carr, and P. Garrou, J. Electron. Mater. **19**, 1357–1364 (1990).

[28] C. F. Kane and R. R. Krchnavek, IEEE Photon. Technol. Lett. **7**, 535–537 (1995).

[29] G. Poberaj, M. Koechlin, F. Sulser, A. Guarino, J. Hajfler, P. Günter, Opt. Mater. **31**, 1054–1058 (2009).

[30] F. Sulser, G. Poberaj, M. Koechlin, P. Günter, Opt. Express **17**, 20291–20300 (2009).

[31] H. Hu, R. Ricken, and W. Sohler, Appl. Phys. B. **98**(4), 677–679 (2010).

[32] H. Hu, L. Gui, R. Ricken, W. Sohler, Proc. SPIE **7604**, Article 76040R (2010), DOI: 10.1117/12.842674.

[33] H. Hu, R. Ricken, and W. Sohler, in: Proceedings of the 14th European Conference on Integrated Optics (ECIO'08), Eindhoven, Netherlands, 2008, pp. 75–78.

[34] M. Koechlin, G. Poberaj, P. Günter, Rev. Sci. Instrum. **80**, 085105-1–5 (2009).

[35] H. Hu, D. Buechter, R. Ricken, and W. Sohler, in: Proceedings of the 15th European Conference on Integrated Optics (ECIO 10), Cambridge, UK, 2010, paper FrPD3,.

[36] R. Regener and W. Sohler, Appl. Phys. B **36**(3), 143–147 (1985).

[37] H. Hu, R. Ricken, and W. Sohler, Opt. Express **17**(26), 24261–24268 (2009).

[38] Z. M. Zhu and T. G. Brown, Opt. Express **10**(17), 853–864 (2002).

[39] E. Dulkeith, F. N. Xia, L. Schares, W. M. J. Green, and Y. A. Vlasov, Opt. Express **14**(9), 3853–3863 (2006).

[40] see Lumerical Solutions, http://www.lumerical.com/, date of last visit: 7 February 2012.

[41] A. Sakai, G. Hara, and T. Baba, Jpn. J. Appl. Phys. 2 **40**(4B), L383–L385 (2001).

[42] D. Duchesne, P. Cheben, R. Morandotti, B. Lamontagne, D. X. Xu, and S. Janz, Opt. Eng. **46** (10), 104602 (2007).

[43] D. E. Zelmon, D. L. Small, and D. Jundt, J. Opt. Soc. Am. B **14**(12), 3319–3322 (1997).

[44] H. Hu, D. Büchter, L. Gui, H. Suche, V. Quiring, R. Ricken, H. Herrmann, and W. Sohler, in: Proceedings of the IEEE Photonic Society 23rd Annual Meeting, Denver, USA, 2010, pp. 254–255.

[45] M. Koechlin, F. Sulser, Z. Sitar, G. Poberaj, P. Günter, IEEE Photon. Technol. Lett. Vol. **22**, 251–253 (2010).

[46] F. Lacour, N. Courjal, M.-P. Bernal, A. Sabac, C. Bainier, M. Spajer, Opt. Mater. **27**, 1421–1425 (2005).

[47] M. Roussey, M.-P. Bernal, N. Courjal, D. Van Labeke, F. I. Baida, Appl. Phys. Lett. **89**, 241110 (2006).

[48] J. Amet, F. I. Baida, G. W. Burr, M.-P. Bernal, Photon. Nanostruct. Fundam. Appl. **6**, 47–59 (2008).

[49] G. W. Burr, S. Diziain, M.-P. Bernal, Opt. Express **16**, 6302–6316 (2008).

[50] S. G. Johnson, S. Fan, P. R. Villeneuve, J. D. Joannopoulos, Phys. Rev. B **60**, 5751–5758 (1999)